Supplementary Material

Dating Late Pleistocene pluvial lake shorelines in the Great Basin, USA using rock surface luminescence dating techniques: developing new approaches for challenging lithologies

Christina M. Neudorf[1, 2], Teresa Wriston[2], Geraint T.H. Jenkins[3], Sebastien Huot[4]

[1]*Vicus, Brisbane, QLD, 4106, Australia*
[2]*Division of Earth and Ecosystem Sciences, Desert Research Institute, Reno, 89512, United States*
[3]*Coventry University, Coventry, CV1 5FB, United Kingdom*
[4]*Illinois State Geological Survey, Champaign Illinois, 61820, United States*
Correspondence to: Christina M. Neudorf (c.neudorf@vicus.net.au)

1. Study sites

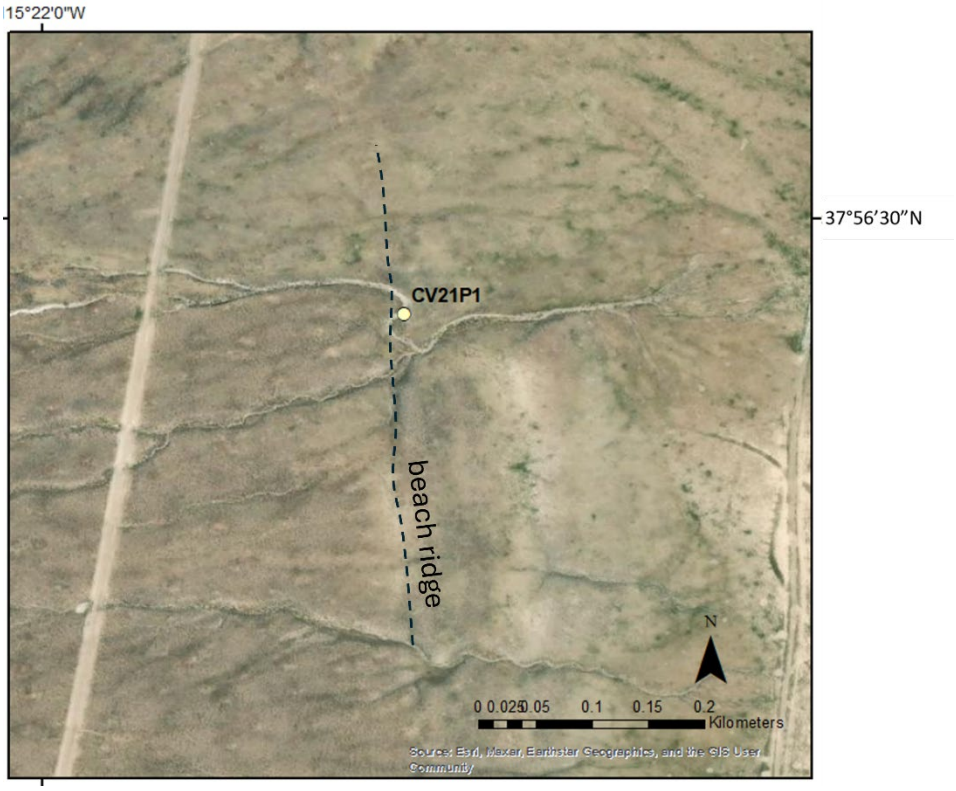

Figure S1. The location of study site CV21P1 on the highest shoreline feature in western Coal Valley. Basemap: ESRI Maxer, Earthstar Geographics, and the GIS User Community.

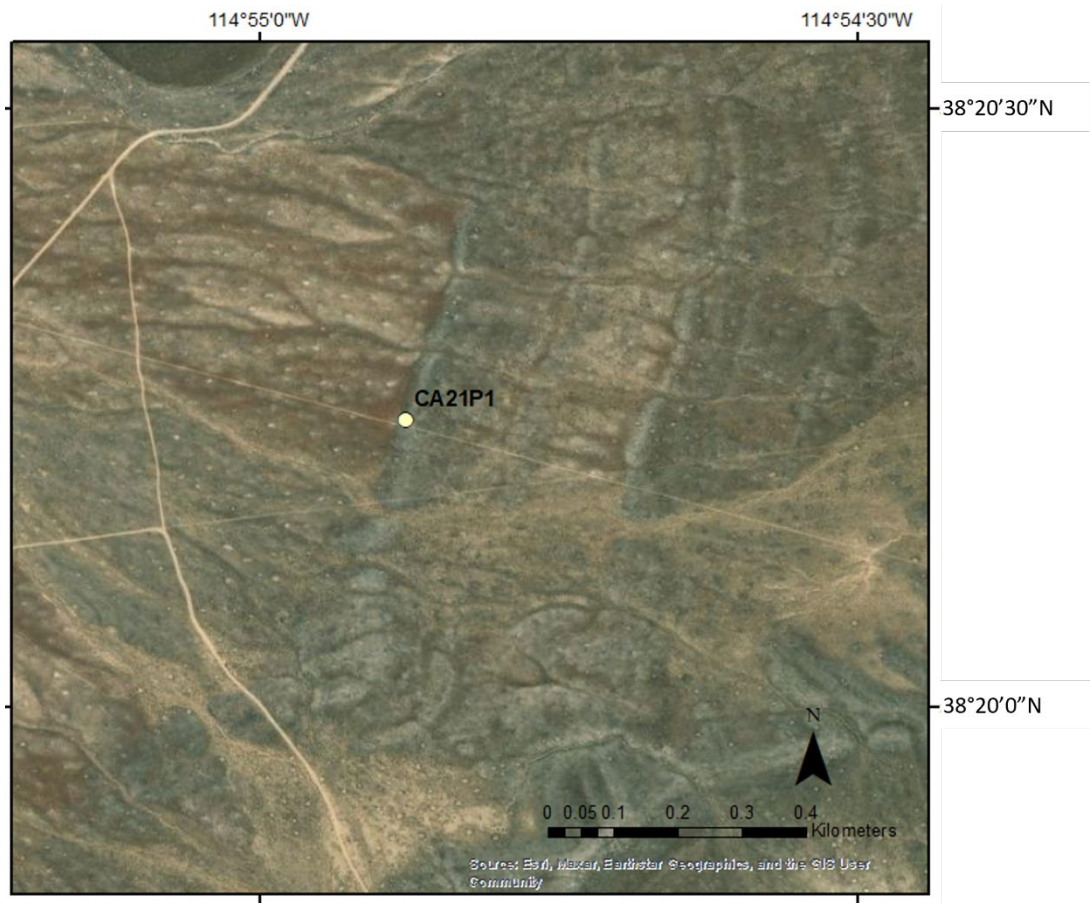

Figure S2. The location of study site CA21P1 on the highest shoreline feature in western Cave Valley. Basemap: ESRI Maxer, Earthstar Geographics, and the GIS User Community.

Figure S3. The location of CA21P2 on a high shoreline feature in southwestern Cave Valley. Basemap: ESRI Maxer, Earthstar Geographics, and the GIS User Community.

Figure S4. The location of study site LK21P1 on the highest shoreline feature in western Lake Valley. Basemap: ESRI Maxer, Earthstar Geographics, and the GIS User Community.

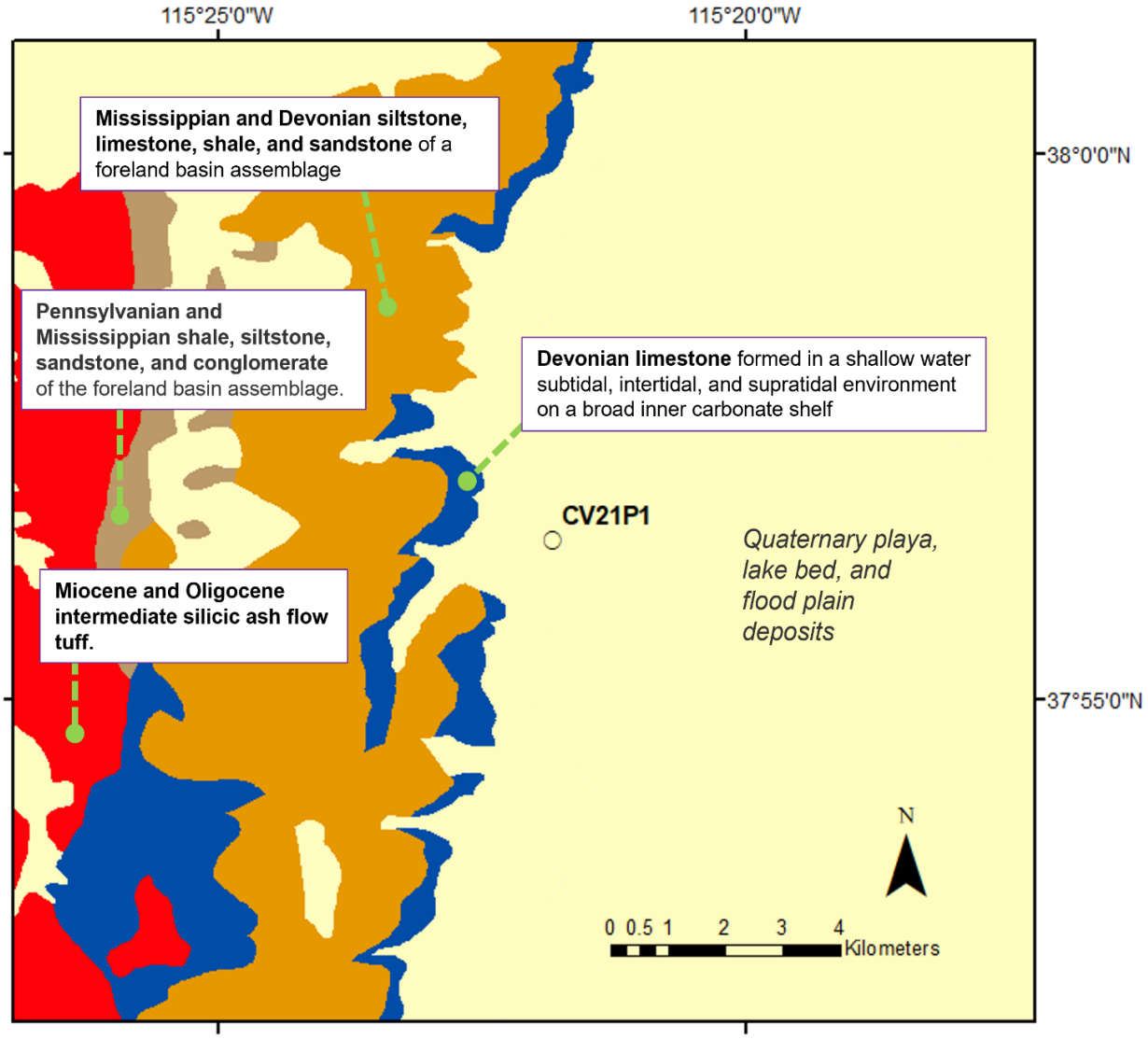

Figure S5. Site CV21P1 is located east of the Guilmette Formation (Devonian limestone) and the Joana, Mercury and Bristol Pass Limestones (Mississippian and Devonian foreland basin assemblage). Generalized surficial geology after Crafford (2007), scale 1:250,000.

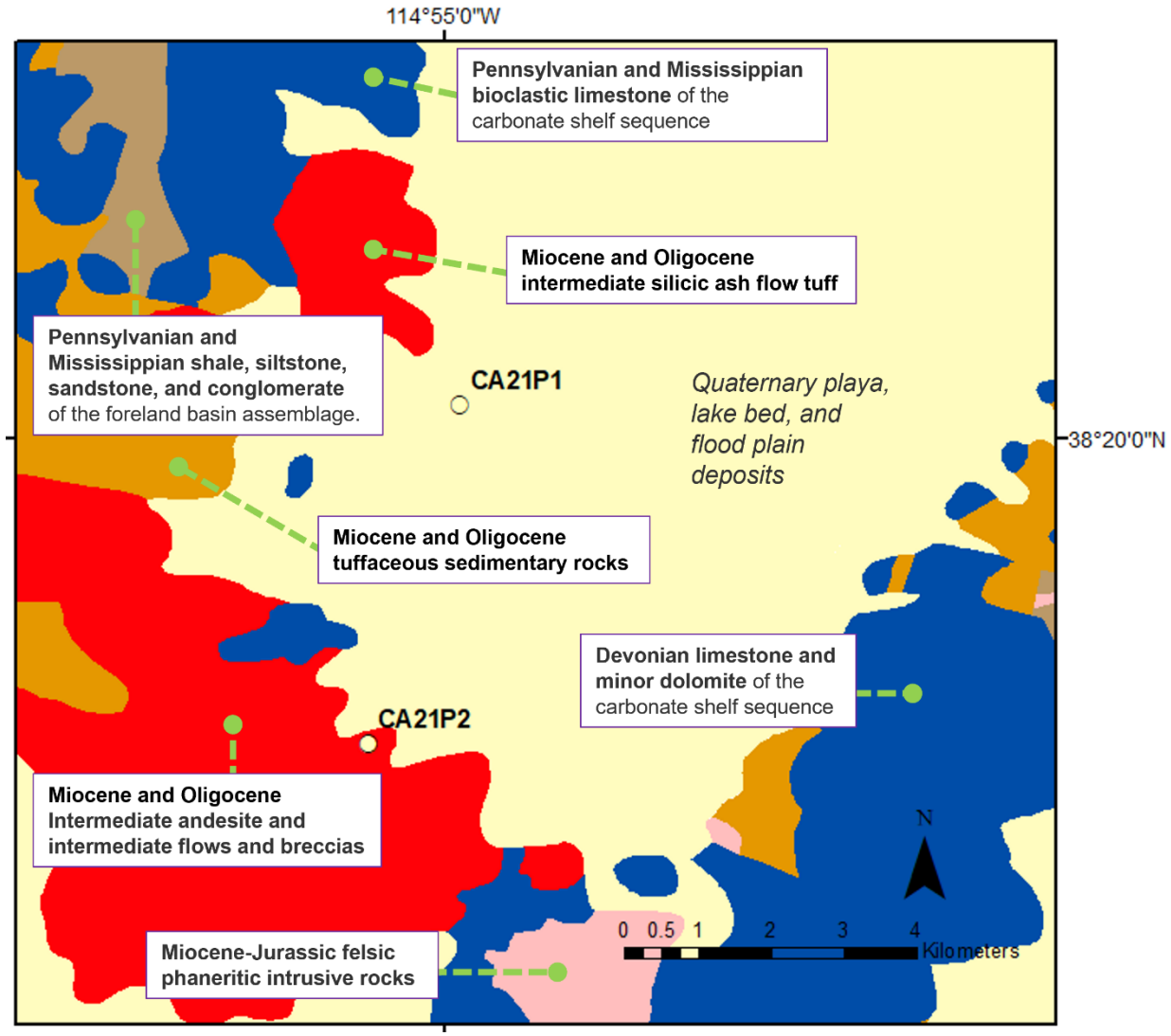

Figure S6. Sites CA21P1 & 2 east of undifferentiated older volcanics with pockets of Pennsylvanian limestone as well as Scotty's Wash quartzite and Chainman shale of upper Mississippian age in the Egan Range. Generalized surficial geology after Crafford (2007), scale 1:250,000.

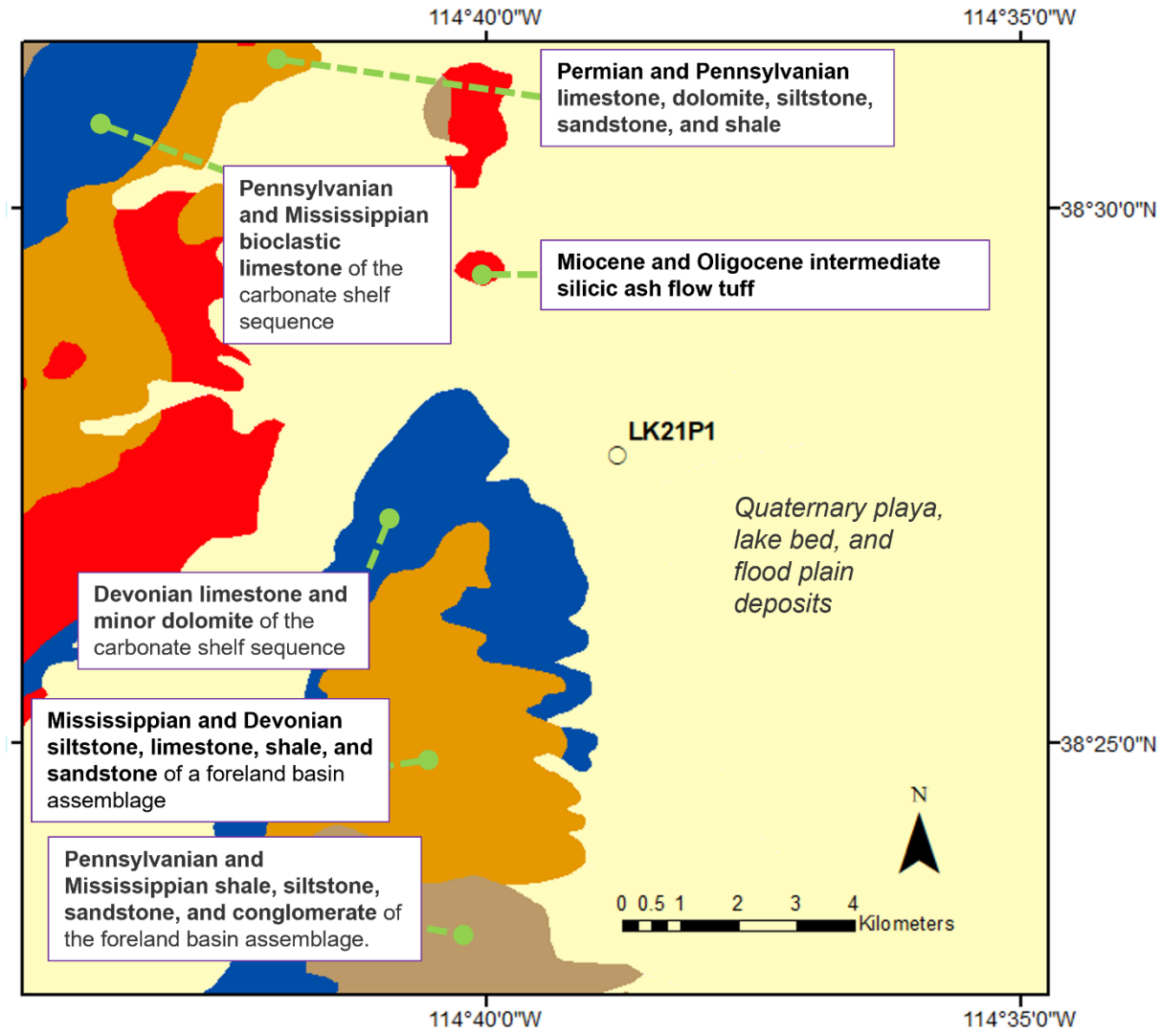

Figure S7. Site LK21P1 located east of middle to upper Devonian Guilmette formation Dolomite and Devils Gate Limestones. Generalized surficial geology from Crafford (2007), scale 1:250,000.

2. SAR protocols tested on volcanic rocks

Table S1. Lower-temperature (180°C & 225°C) pIRIR protocols tested in this study.

Step	pIRIR180 (multi-grain)	pIRIR225 (multi-grain)
1	Natural/Regenerative Dose	Natural/Regenerative Dose
2	Preheat (200°C, 10 s)	Preheat (250°C, 10 s)
3	IR diodes (50°C, 100 s)	IR diodes (50°C, 100 s)
4	IR diodes (180°C, 100 s) → *Ln*, *Lx*	IR diodes (225°C, 100 s) → *Ln*, *Lx*
5	Test dose (~10 Gy)	Test dose (~10 Gy)
6	Preheat (200°C, 10 s)	Preheat (250°C, 10 s)
7	IR diodes (50°C, 100 s)	IR diodes (50°C, 100 s)
8	IR diodes (180°C, 100 s) → *Tn*, *Tx*	IR diodes (225°C, 100 s) → *Tn*, *Tx*
9	IR diodes (200°C, 40 s)	IR diodes (290°C, 40 s)
10	Return to step 1.	Return to step 1.

3. CW- and LM-OSL measurements

3.1 Continuous wave measurements

Standard *De* measurement from quartz extracts typically involves continuous wave (CW) light stimulation at 125℃ and luminescence detection using UV filters with emissions centered at 365 nm. If contamination from feldspar is anticipated, such as we expect in our polymineral samples, blue light stimulation is often preceded by stimulation with infrared (IR) diodes to bleach any signal contribution from feldspar without further bleaching the signal from quartz (also known as a post-IR OSL measurement, Roberts, 2007). For sediment extracts from samples in this study, both the OSL (here meaning optically stimulated luminescence detected during blue light stimulation) and the post-IR OSL were measured to determine if there is a signal from quartz that can be isolated from feldspar signal contamination using an IR bleach (Tables S2-S4). Samples with signals coming mainly from quartz were expected to have OSL and the post-IR OSL signals of similar intensity implying negligible signal reduction due to IR bleaching of feldspar. Samples with signals coming mainly, or in part, from contaminating feldspar were expected to have post-IR OSL signals that are less intense than the OSL signals, as well as a prominent IR signal. In some samples, neither the IR signal from feldspar, nor the OSL signal from quartz yielded a detectable signal.

Coal Valley CW signals

Most Coal Valley samples measured from limestone rocks exhibited OSL signals that were drastically reduced after IR stimulation (e.g., Rock 11, Table S2). Thus, we concluded that quartz minerals within the limestones are not reliable for dating and further testing should focus on the IR signals from feldspar. Some limestone gravels collected from site CV21P1 yielded minerals with a clear IR signal with photon counts of 800 counts/second or more (e.g., Rock 11, Table S2).

Cave Valley CW signals

In the case of the volcanic rocks from Cave Valley, OSL and post-IR OSL signals were often similar in intensity, though many rocks did not have a detectable IRSL signal (e.g., Rock 1, Table S3). Out of 20 rocks tested, 7 exhibited a detectable IRSL signal and photos of these rocks after sample preparation

are shown in Supplementary Material Section 4 below. Volcanic rocks with the brightest signals (typically with bright IR signals, e.g., Rock 4, Table S3) were typically of the felsic (andesitic or rhyolitic) varieties, whereas basalts, like those collected from site CA21P2, had no signal (Table S4).

3.2 LM-OSL measurements

LM-OSL curves (Bulur, 1996) were measured from a subset of limestone and volcanic gravel sediment extracts (Tables S2-S4). Each LM-OSL signal was measured with blue LEDs where the stimulation power was ramped from 0 to 90% over 3600 s and each LM-OSL measurement was preceded by an IR stimulation at 50°C to deplete any signal from contaminating feldspars. No fast component was detected from quartz in any of the polymineral samples obtained from limestone or volcanic rocks, suggesting that further testing should focus on the IR signal from feldspar in both rock lithologies.

Table S2. OSL, IRSL, post-IR OSL and LM-OSL signals for limestone sediment extracts from Rocks 11 and 14 from Coal Valley site CV21P1. The UV filter is used to detect 365 nm wavelength luminescence emissions from quartz (or contaminating feldspar using IR stimulation), while the violet filter detects 410 nm wavelength emissions from feldspar.

Rock sample	Detection filter		
	UV filter (U-340)	Violet filter (Schott BG-3 & BG39)	UV filter (U-340)
Rock 11	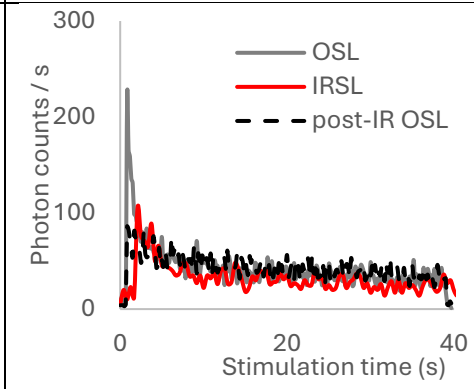	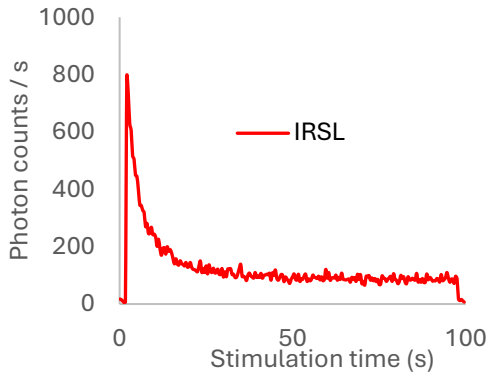	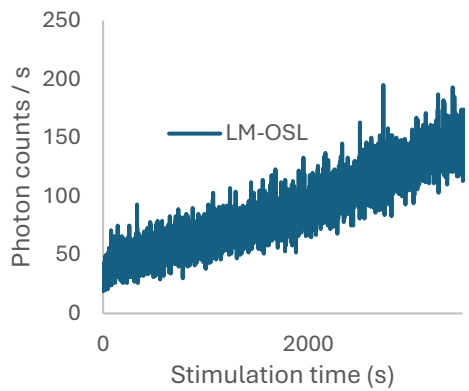
Rock 14	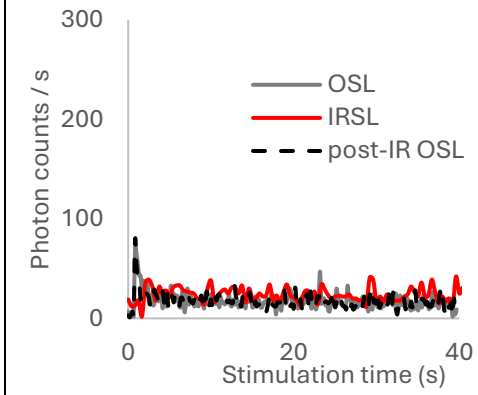	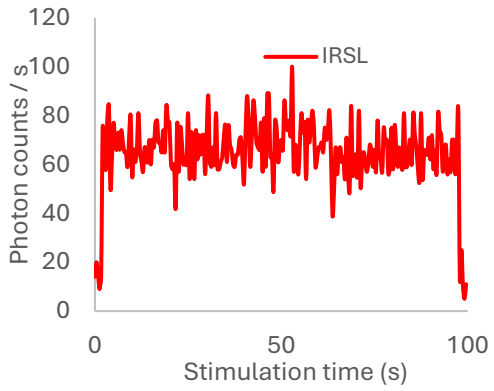	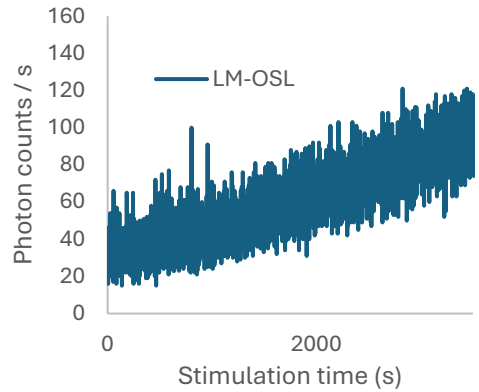

Table S3. OSL, IRSL, post-IR OSL and LM-OSL signals for Rocks 1 and 4 from Cave Valley site CA21P1. The UV filter is used to detect 365 nm wavelength luminescence emissions from quartz (or contaminating feldspar using IR stimulation), while the violet filter detects 410 nm wavelength emissions from feldspar.

Rock sample	Detection filters		
	UV filter (U-340)	Violet filter (Schott BG-3 & BG39)	UV filter (U-340)
Rock 1	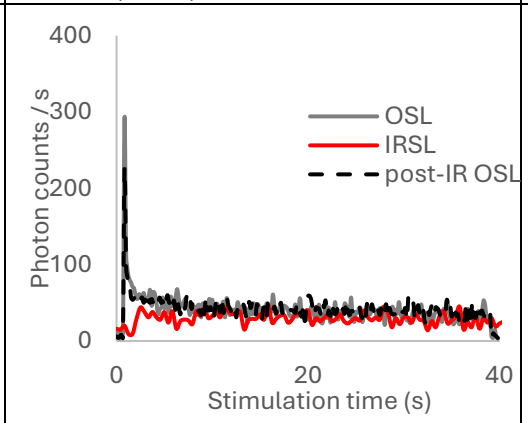	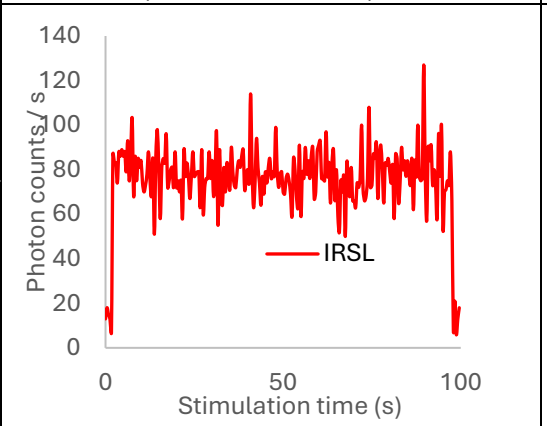	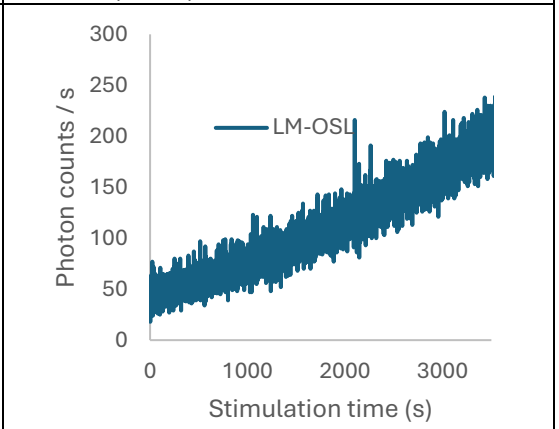
Rock 4	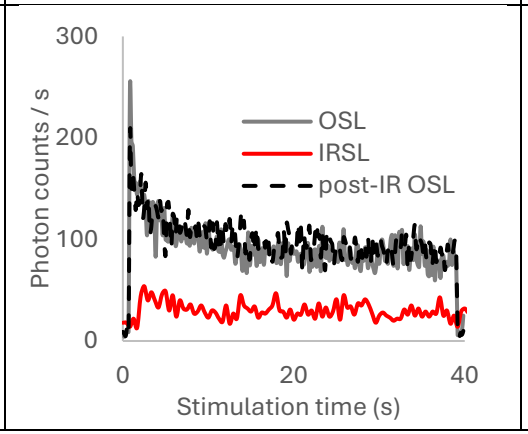	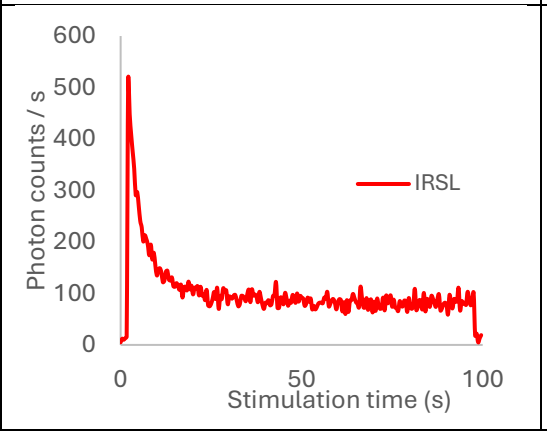	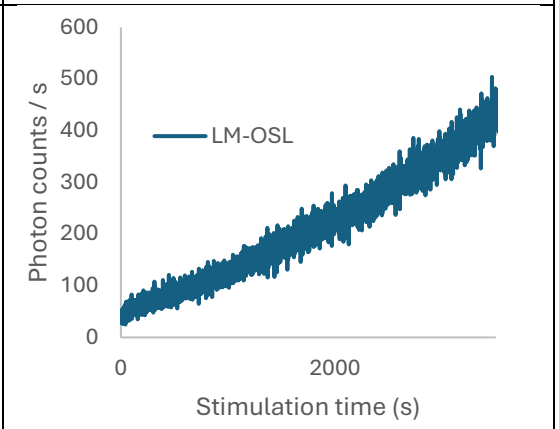

Table S4. OSL, IRSL, post-IR OSL and LM-OSL signals for 2 volcanic rocks from Cave Valley site CA21P2. The UV filter is used to detect 365 nm wavelength luminescence emissions from quartz (or contaminating feldspar using IR stimulation), while the violet filter detects 410 nm wavelength emissions from feldspar.

Rock Sample	Detection filters		
	UV filter (U-340)	Violet filter (Schott BG-3 & BG39)	UV filter (U-340)
Rock 1	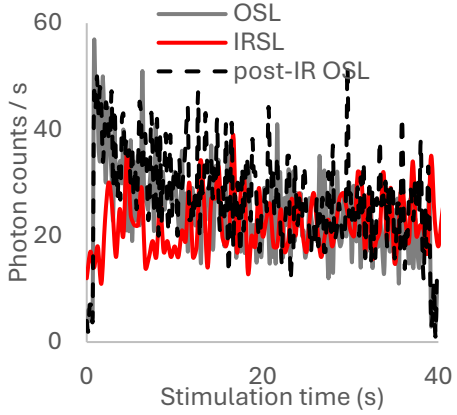	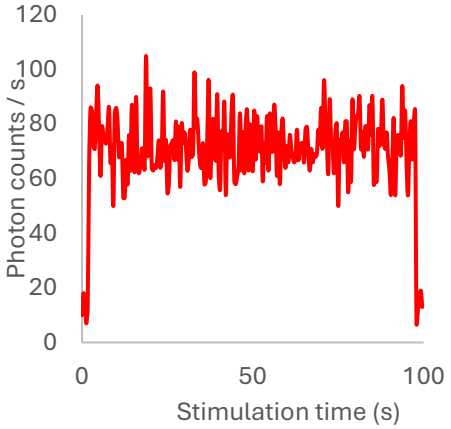	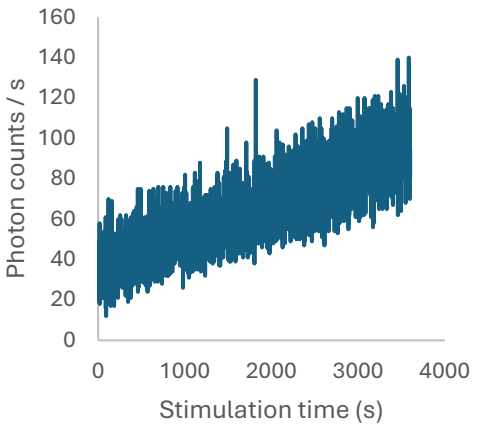
Rock 2	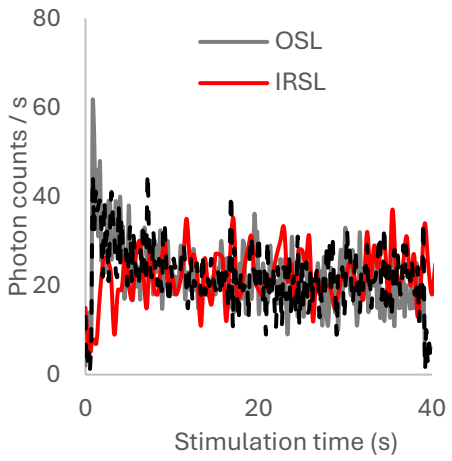	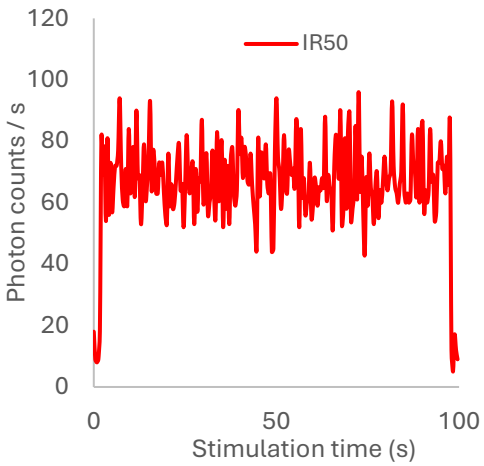	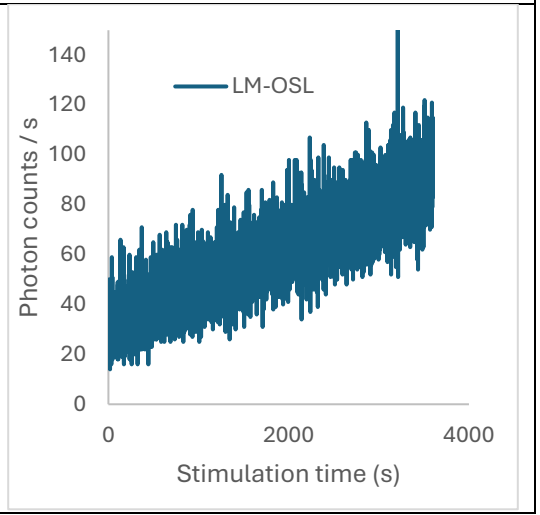

4. Cored volcanic rocks from site CA21P1, Cave Valley

A) Rock 4

B) Rock 7

C) Rock 11

D) Rock 12

E) Rock 13

F) Rock 14

G) Rock 18

Figure S8. Rocks sampled for signal testing and dating from site CA21P1. Photos have been taken after core extraction and dremeling of the surface. Rock 14 was found to be chert (cryptocrystalline quartz) and was not dated.

5. Dose recovery test results

A) Rock 2 (63-90 µm fraction), n=285

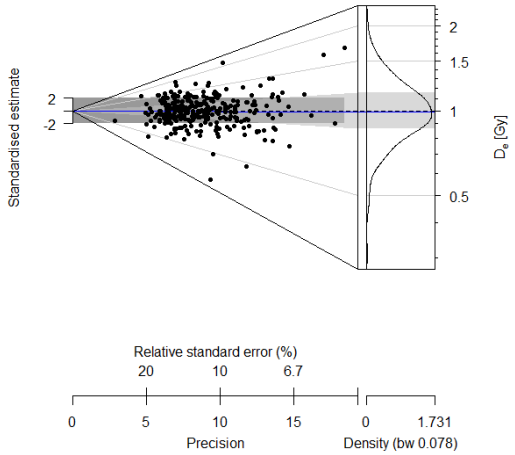

B) Rock 10 (125-180 µm fraction), n=50

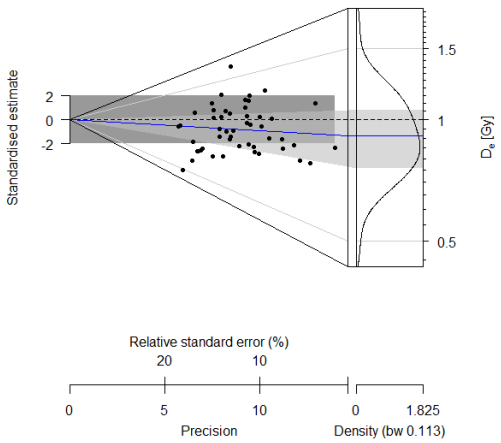

C) Rock 18 (180-250 µm fraction), n=53

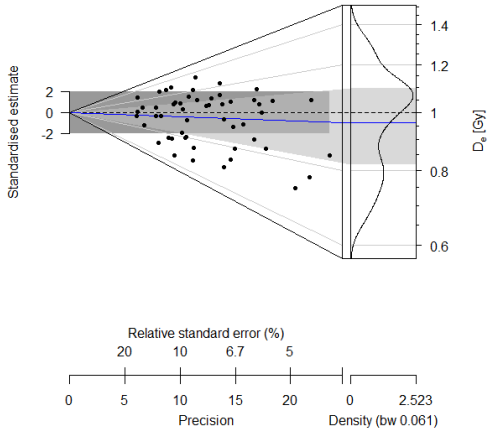

Figure S9. Dose recovery test results for polyminerals extracted from limestone clasts of CV21P1. Abanico plots were generated using the "Luminescence" R package (Dietze, 2021; Dietze and Kreutzer, 2021).

A)

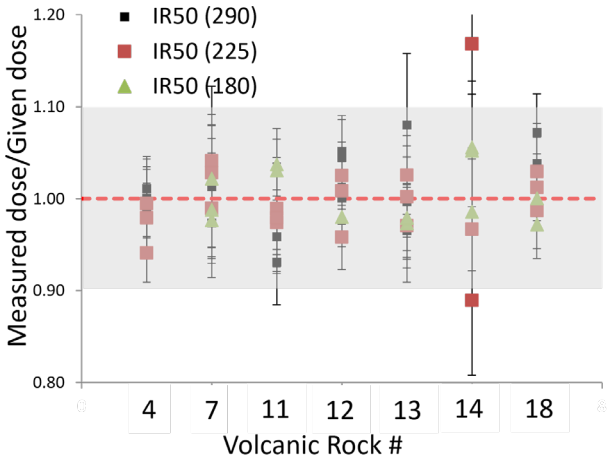

B)

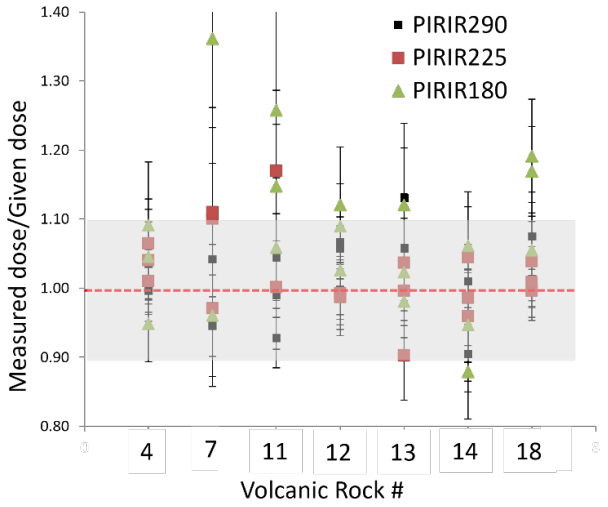

Figure S10. Dose recovery test results for volcanic rocks collected from site CA21P1 in Cave Valley using IR50 signals (A) and pIRIR signals (B). Each dot represents one 3 mm diameter multi-grain aliquot. Measured/given dose ratios that fall within 10% of unity (grey shading) are considered favorable and evidence that the SAR protocol is suitable for the sample.

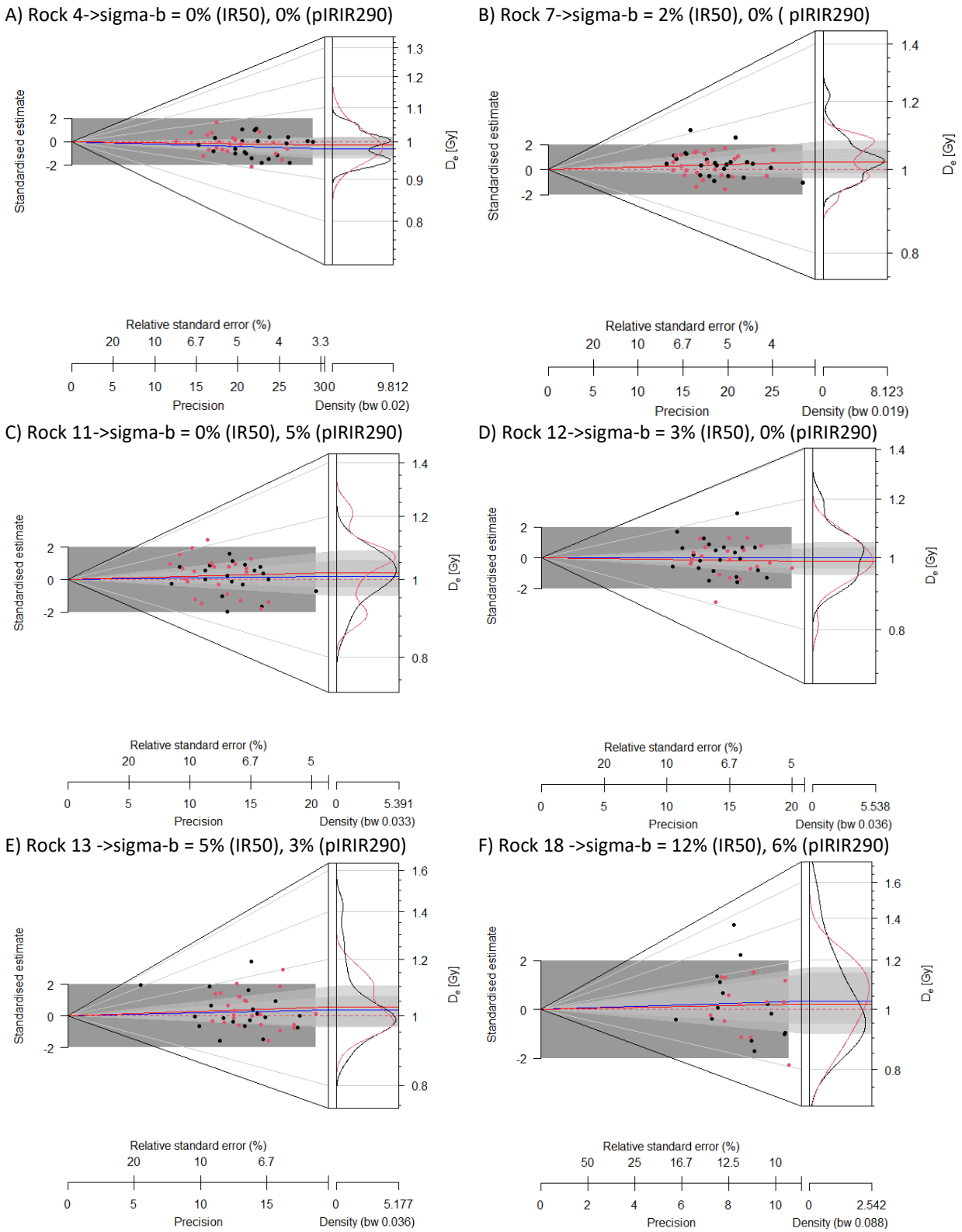

Figure S11. Dose recovery test results for the ground and suspension settled 32-63 µm fraction of volcanic rocks 4, 7, 11, 12, 13, 18 from CA21P1 in Cave Valley. A minimum of 24 multi-grain aliquots were measured and results include aliquots that passed SAR aliquot rejection criteria. Black dots are measured/given dose ratio values for the IR50 signal, and red dots are those for the pIRIR290 signal. Abanico plots were generated using the "Luminescence" R package (Dietze, 2021; Dietze and Kreutzer, 2021).

6. Fading measurements and corrections

A) Rock 2 (63-90 µm)

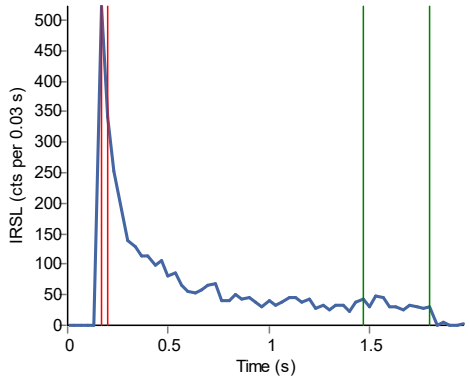

B) Rock 2 (63-90 µm)
g-value = 2.31 ± 3.24 %/decade

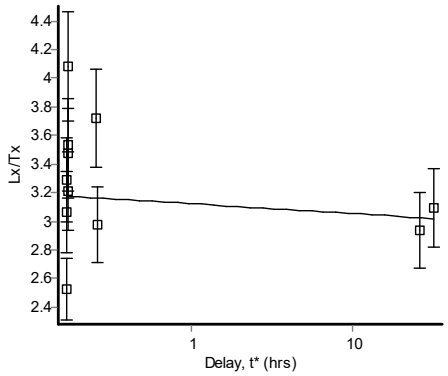

C) Rock 10 (125-180 µm)

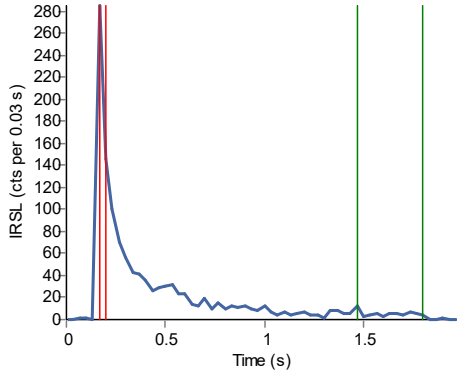

D) Rock 10 (125-180 µm)
g-value = 27.34 ± 4.33 %/decade

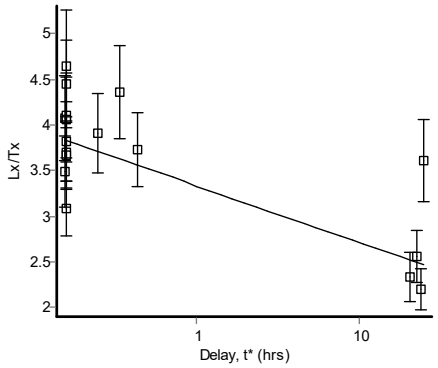

E) Rock 18 (180-250 µm)

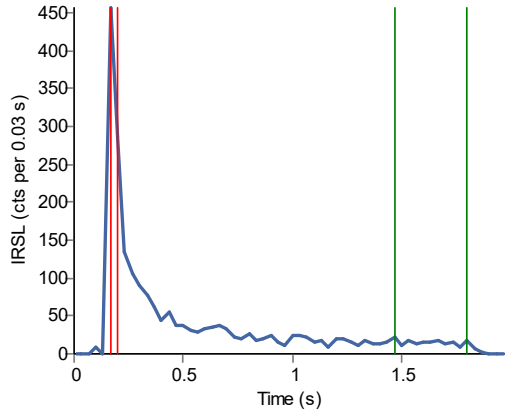

F) Rock 18 (180-250 µm)
g-value = 3.27 ± 3.80 %/decade

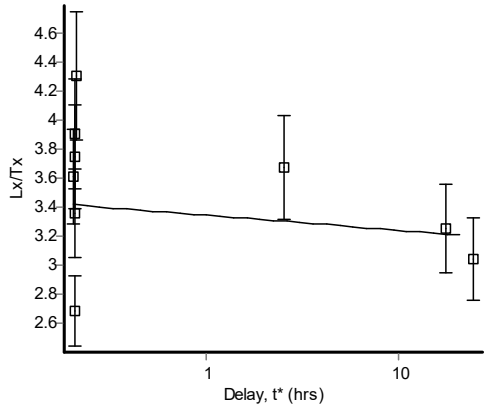

Figure S12. Coal Valley CV21P1 sample IR50 signals from a single grain from each rock (left) and fading measurement results from the same grain (right). Signal fading approximates a log-linear rate.

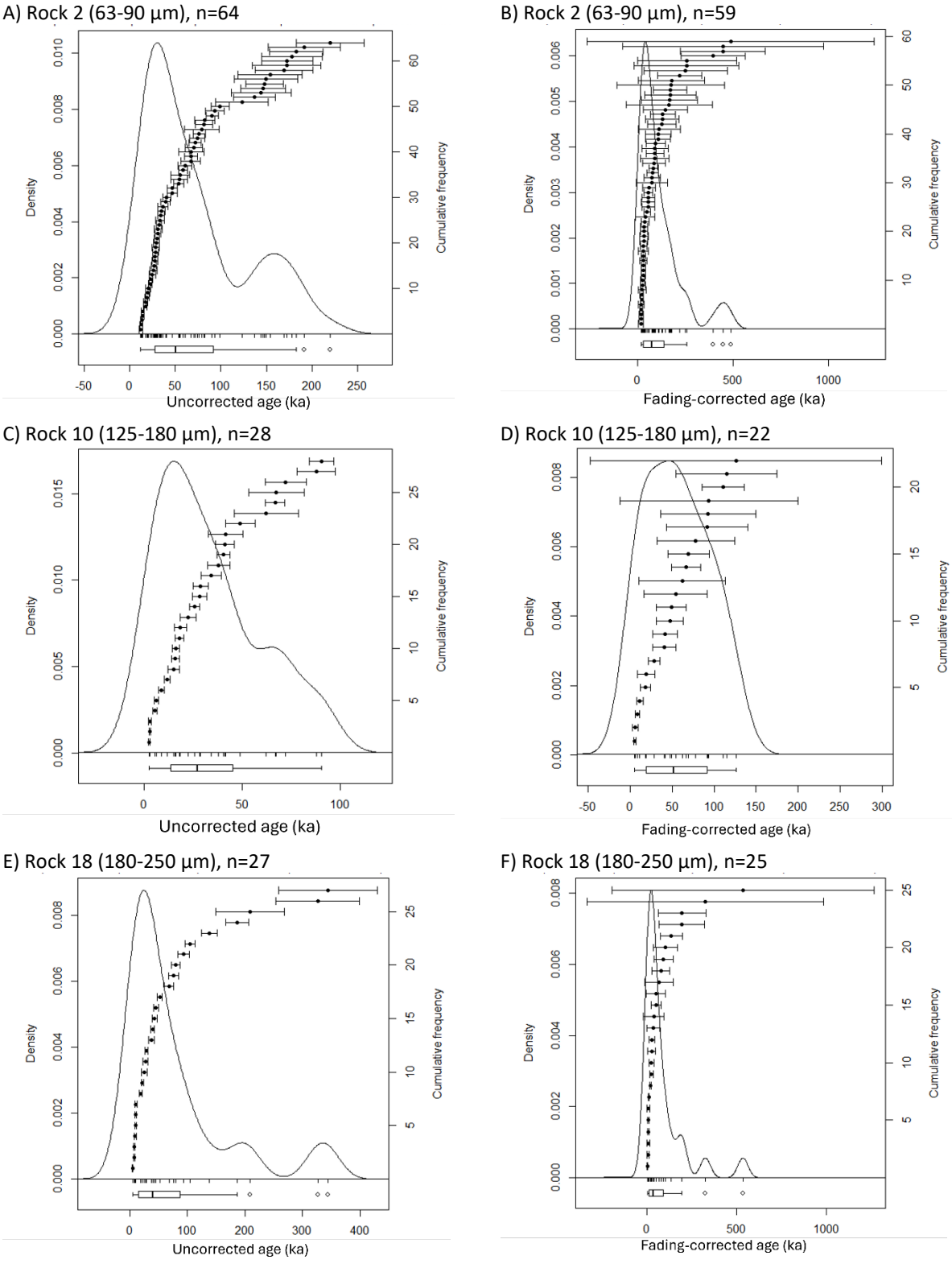

Figure S13. Uncorrected (left) and fading-corrected (right) aliquot age distributions for limestone Rocks 2, 10 and 18 from CV21P1 in Coal Valley. The cumulative distribution plot is superimposed on a kernel density estimate (KDE) curve. All grains were corrected for their own fading rate using the model of Huntley and Lamothe (2001). Grains with fading rates >10%/decade were rejected from analysis before fading correction.

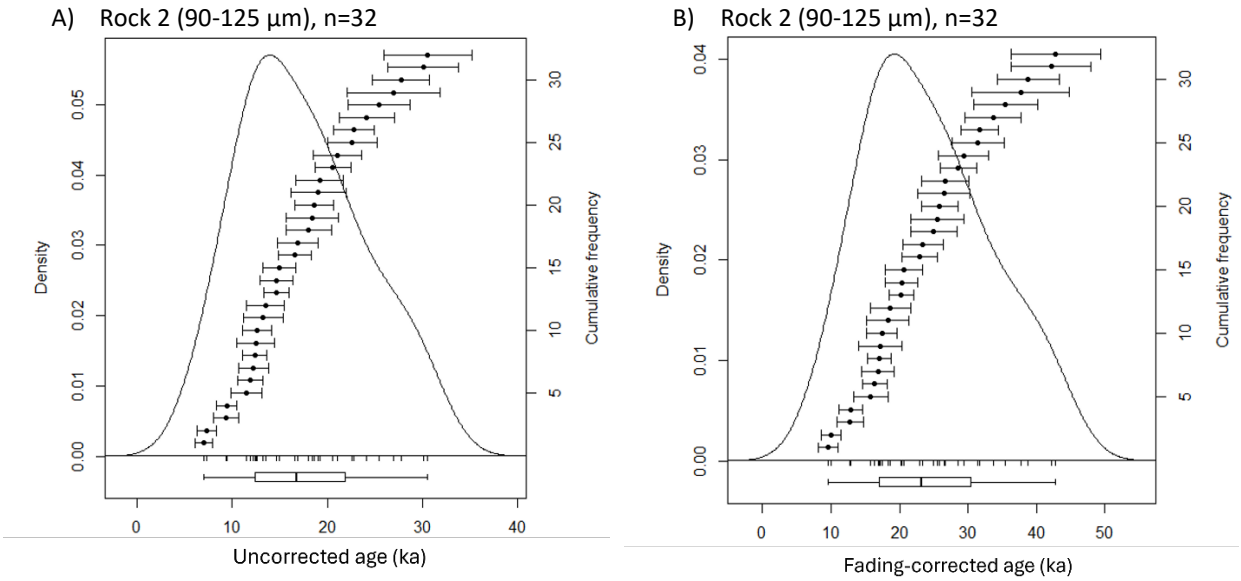

Figure S14. The uncorrected (A) and fading-corrected (B) age distribution for the 90-125 µm grain size fraction from Rock 2 of CV21P1. All aliquots were corrected using an average fading rate of 3.19 ± 0.15 %/decade measured from four 2 mm diameter aliquots.

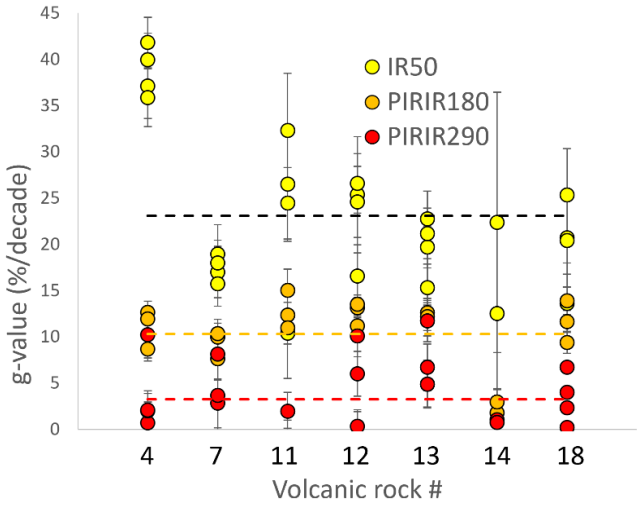

Figure S15. Measured fading rates for volcanic rocks collected from site CA21P1 in Cave Valley. Each dot represents one 3 mm diameter multi-grain aliquot. Black, yellow and red dashed lines mark the weighted mean g-values for the IR50, $pIRIR_{180}$ and pIRIR290 signals, respectively.

Table S5. CA21P1 volcanic rock dose rates, fading rates and *ρ'* values. *g*-values were measured using the approach of Auclair et al. (2003).

Volcanic rock #	Dose rate (Gy/ka)	IR50 g-value (%/decade)	PIRIR290 g-value (%/decade)	PIRIR290 *ρ'*
Rock 4	5.56 ± 0.28	39.0 ± 1.5	3.7 ± 1.5	$1.19e^{-6} \pm 5.26e^{-7}$
Rock 7	6.66 ± 0.39	17.2 ± 1.3	3.5 ± 1.1	$3.72e^{-6} \pm 7.69e^{-7}$
Rock 11	6.74 ± 0.37	22.4 ± 2.5	-0.7 ± 1.7	$2.25e^{-6} \pm 5.0e^{-7}$
Rock 12	6.24 ± 0.13	22.8 ± 1.9	3.9 ± 1.3	$4.16e^{-6} \pm 1.48e^{-6}$
Rock 13	6.36 ± 0.05	19.5 ± 1.3	6.6 ± 1.1	$3.79e^{-6} \pm 7.45e^{-7}$
Rock 18	6.28 ± 0.34	19.7 ± 2.3	3.4 ± 1.7	$5.41e^{-6} \pm 1.50e^{-6}$

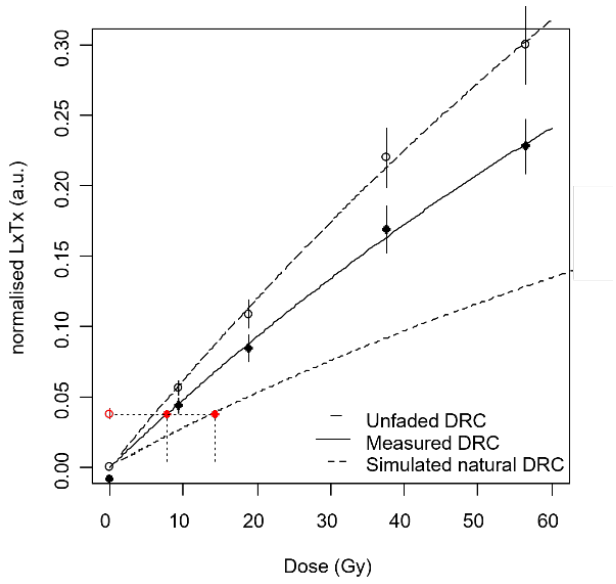

Figure S16. Fading-corrected dose response curve for the pIRIR signal of an aliquot from volcanic Rock 7 from CA21P1. Red dots indicate where the natural (*Ln*/*Tn*) signal is interpolated onto the unfaded and simulated DRCs. Corrections apply the Kars et al. (2008) approach based on the model of Huntley (2006).

7. Radionuclide concentrations

Table S6 Radionuclide concentrations for limestone gravels sampled from site CV21P1 as determined by ICP-MS/AES and HPGe measurements.

Rock sample	Method	U nat (ppm)	Th (ppm)	K (%)	Rb (ppm)
Rock 2	ICP-MS/AES	0.57 ± 0.06	0.77 ± 0.08	0.23 ± 0.03	7.10 ± 0.71
Rock 10	ICP-MS/AES	1.00 ± 0.10	0.19 ± 0.02	0.02 ± 0.01	1.40 ± 0.14
Rock 18	ICP-MS/AES	0.51 ± 0.08	0.72 ± 0.09	0.17 ± 0.02	0.60 ± 0.06
Gravel matrix	ICP-MS/AES	1.61 ± 0.16	2.63 ± 0.26	0.52 ± 0.07	22.5 ± 2.25
Gravel matrix	HPGe	2.12 ± 0.06	0.54 ± 0.01	0.11 ± 0.01	--
Limestones (bulk)	HPGe	0.99 ± 0.14	0.78 ± 0.04	0.14 ± 0.01	--

Table S7. HPGe measurement of homogenized beach ridge sand from Skagen, Denmark (standard #063002).

	Specific activity (Bq/kg)			
	U-238	Th-232	Ra-226	K-40
This study	4.6 ± 0.5	4.5 ± 0.1	4.7 ± 0.1	334 ± 5
Murray et al., 2015	5.0 ± 0.3	3.9 ± 0.5	4.5 ± 0.4	333 ± 10

Table S8. CV21P1 sample radionuclide activity (Bq/kg) ratios for U and Th series determined using HPGe detection.

Sample	Ra-226 vs U-238	Pb-210 vs U-238	Pb-210 vs Ra-226	Ra-224 vs Ac-228
Gravel matrix	1.04 ± 0.03	1.28 ± 0.06	1.23 ± 0.05	0.80 ± 0.08
Limestones	0.93 ± 0.13	1.01 ± 0.30	1.08 ± 0.29	1.02 ± 0.20

Table S9. Volcanic gravel radionuclide contents of CA21P1 samples.

Rock sample	Method	U nat (ppm)	Th (ppm)	K (%)	Rb (ppm)
Rock 4	ICP-MS/AES	5.24 ± 0.52	18.6 ± 1.86	2.85 ± 0.28	139 ± 13.9
Rock 7	ICP-MS/AES	5.14 ± 0.51	21.4 ± 2.14	3.93 ± 0.39	181 ± 18.1
Rock 11	ICP-MS/AES	6.53 ± 0.65	22.5 ± 2.25	3.82 ± 0.38	169 ± 16.9
Rock 12	ICP-MS/AES	5.24 ± 0.52	18.9 ± 1.89	3.73 ± 0.37	171 ± 17.1
Rock 13	ICP-MS/AES	6.70 ± 0.67	21.0 ± 2.10	3.78 ± 0.38	189 ± 18.9
Rock 18	ICP-MS/AES	5.91 ± 0.59	20.6 ± 2.06	3.87 ± 0.39	166 ± 16.6
Gravel matrix	ICP-MS/AES	3.16 ± 0.32	10.9 ± 1.30	2.32 ± 0.23	98.1 ± 9.81
Gravel matrix	HPGe	3.27 ± 0.10	13.4 ± 0.07	2.42 ± 0.23	--

Table S10. Radionuclide activity ratios for the U and Th series determined using HPGe detection for gravel matrix from site CA21P1.

Sample	Ra-226 vs U-238	Pb-210 vs U-238	Pb-210 vs Ra-226	Ra-224 vs Ac-228
Gravel matrix	1.18 ± 0.04	1.39 ± 0.07	1.17 ± 0.04	0.99 ± 0.01

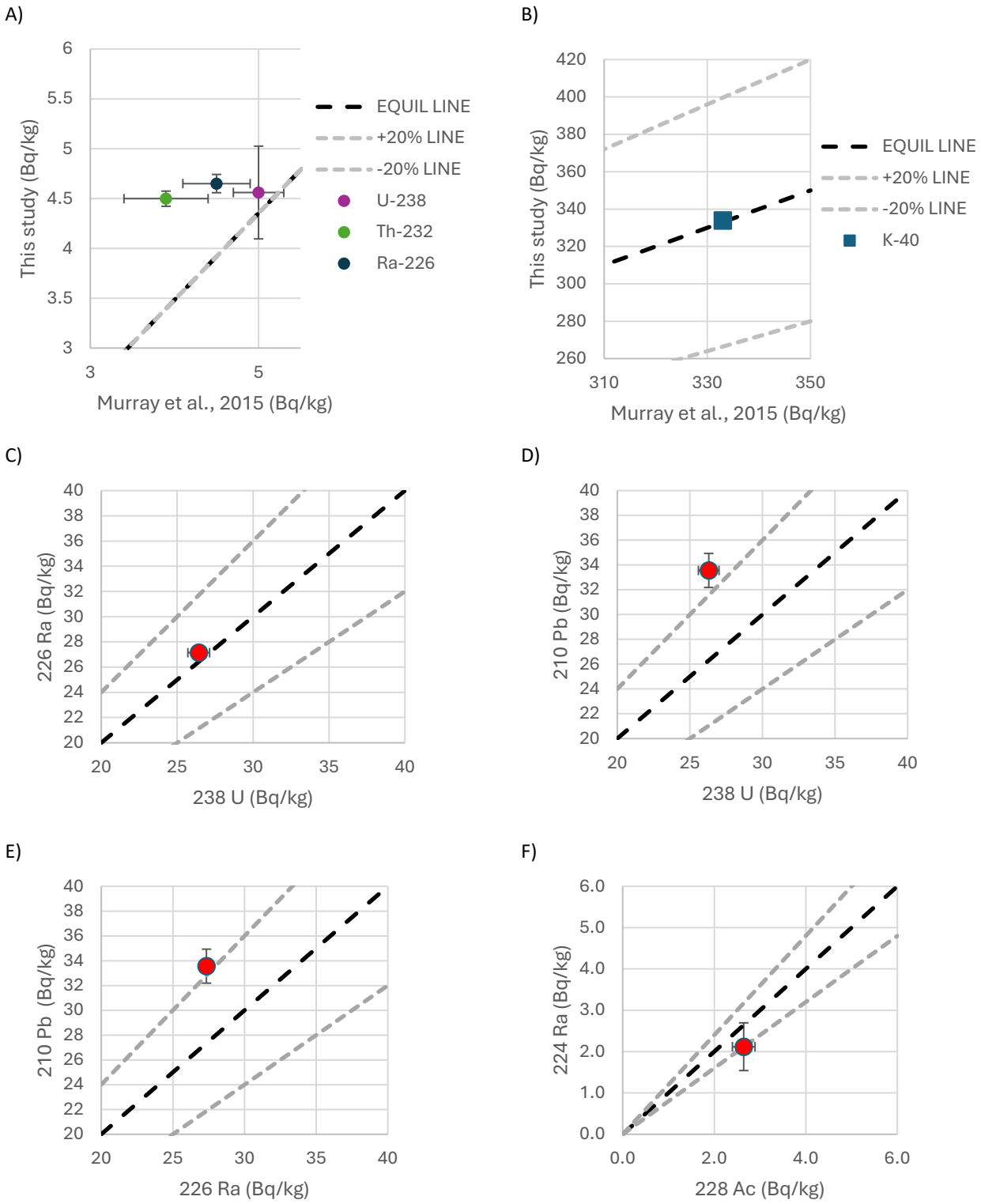

Figure S17. HPGe measurements of calibration standard Skagen 063002 (A & B). Measurements in this study are compared to those of Murray et al. (2015), which report the mean results from 23 laboratories. Our results are within 20% of those previously published. Error bars for K-40 are smaller than the size of the symbol. (C-F) Radionuclide activity ratios for the gravel matrix sample from site CV21P1. Grey dashed lines delineate ±20% of unity.

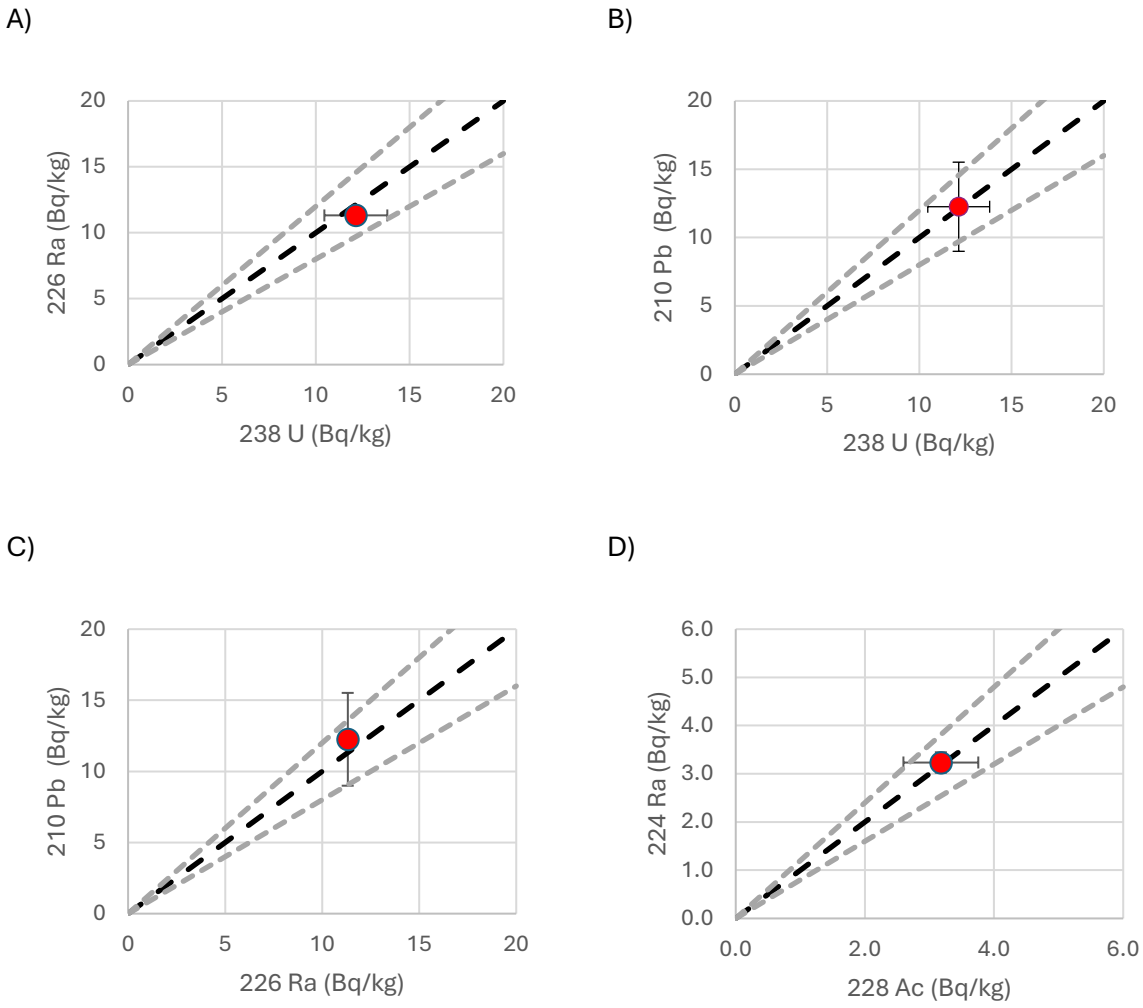

Figure S18. Radionuclide activity ratios for the limestone sample from site CV21P1. Grey dashed lines delineate ±20% of unity.

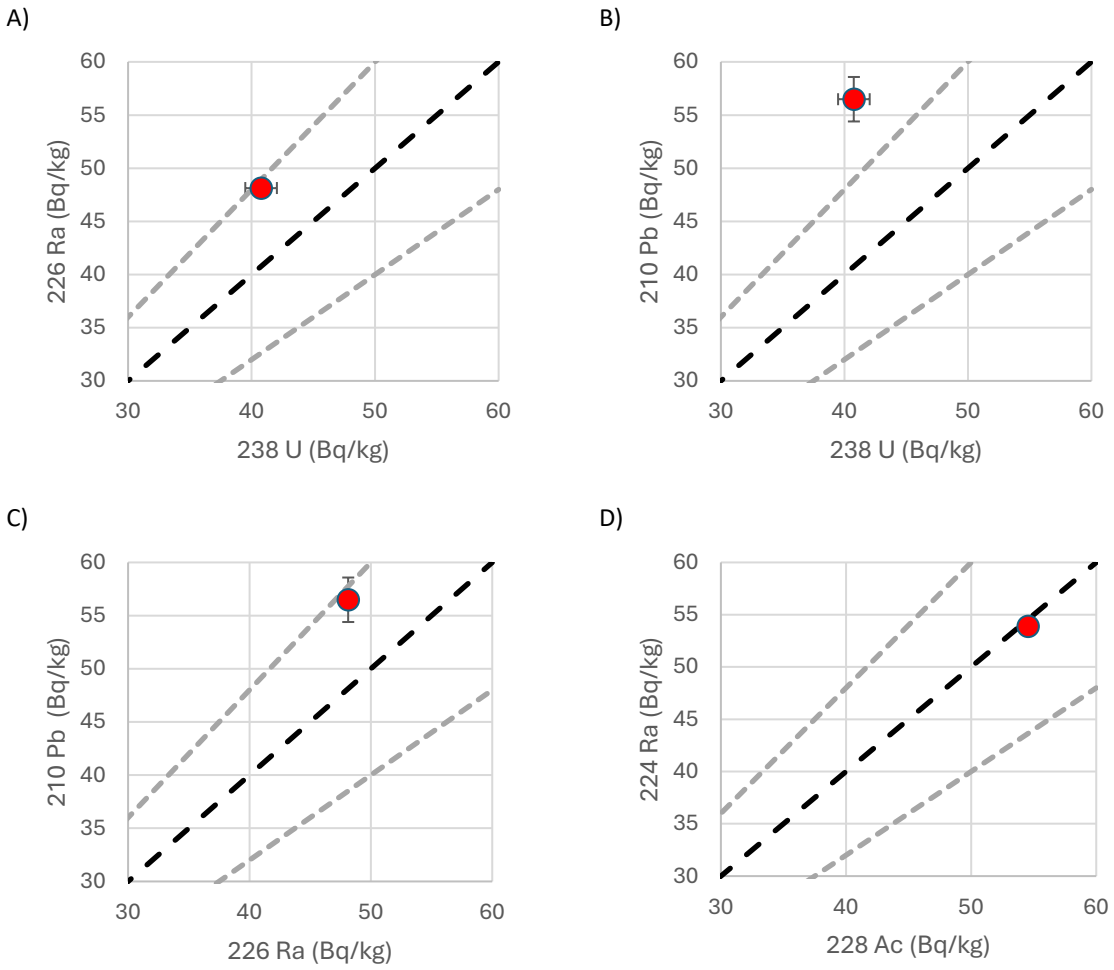

Figure S19. Radionuclide activity ratios for the U and Th series determined using HPGe detection for gravel matrix from site CA21P1.

8. SEM analysis

A) ROCK 4

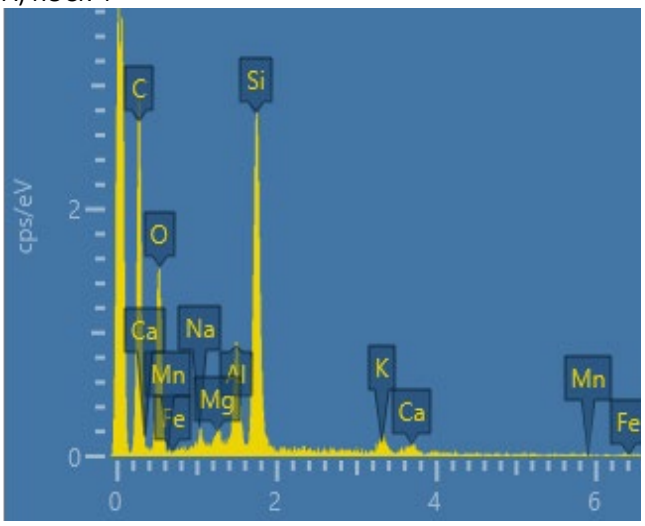

B) ROCK 4

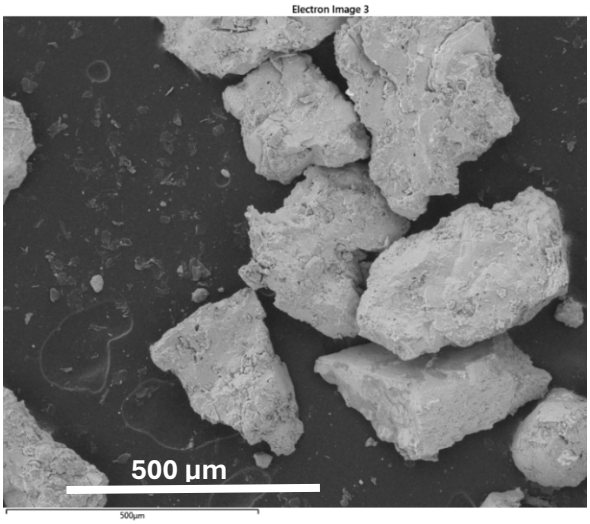

C) ROCK 7

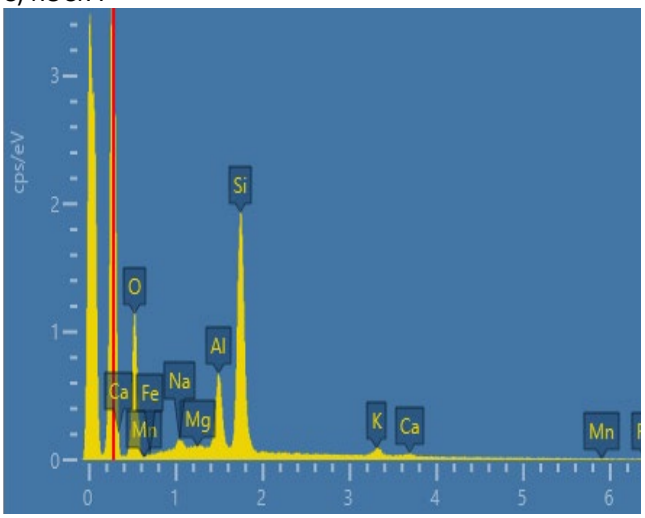

D) ROCK 7

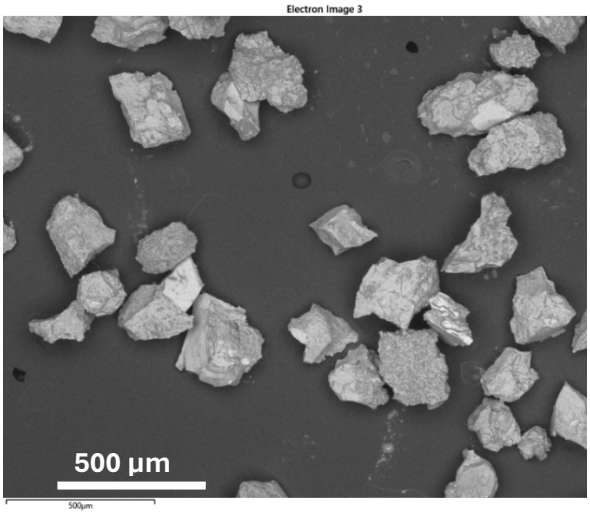

Figure S20. EDS-SEM data for volcanic Rocks 4 and 7. EDS spectra (left) showing the presence of K. Backscatter SEM images (right) of grains from sieved and crushed rock slices from CA21P1.

A) ROCK 12

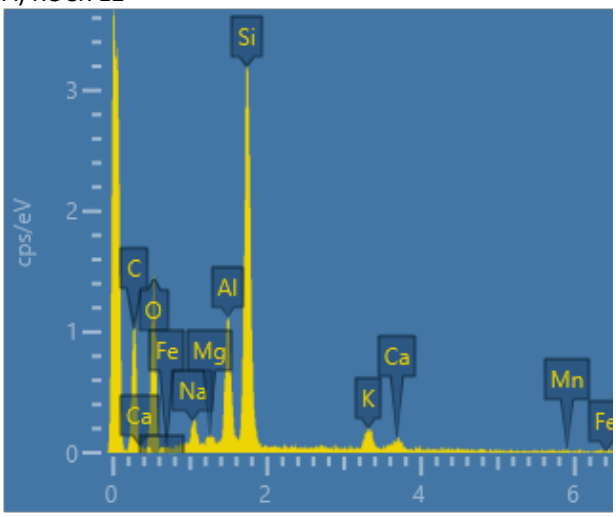

B) ROCK 12

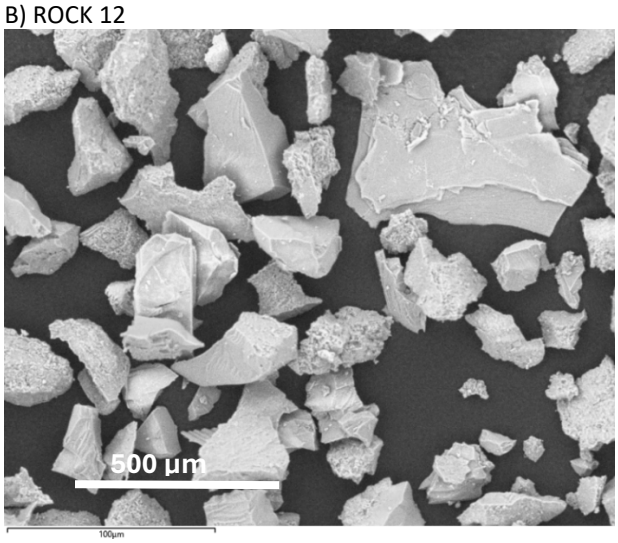

C) ROCK 13

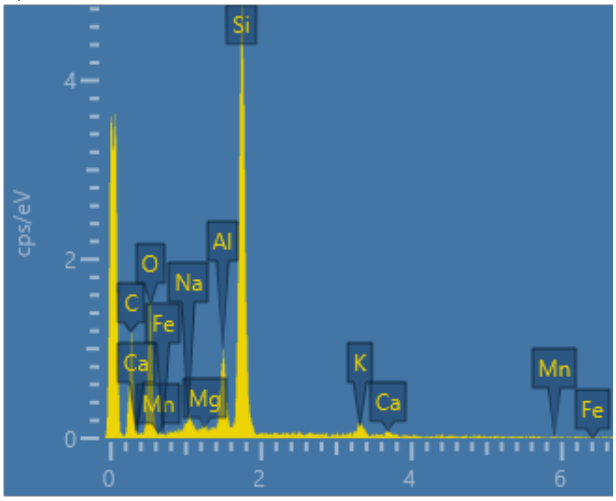

D) ROCK 13

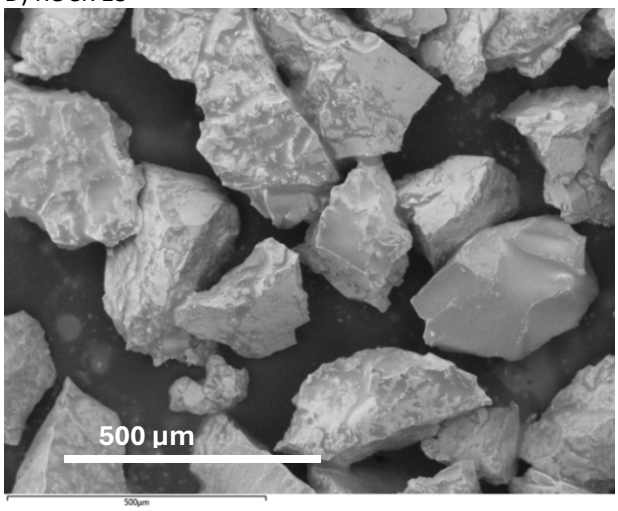

Figure S21. EDS-SEM data for volcanic Rocks 12 and 13. EDS spectra (left) showing the presence of K. Backscatter SEM images (right) of grains from sieved and crushed rock slices from CA21P1.

A) ROCK 18

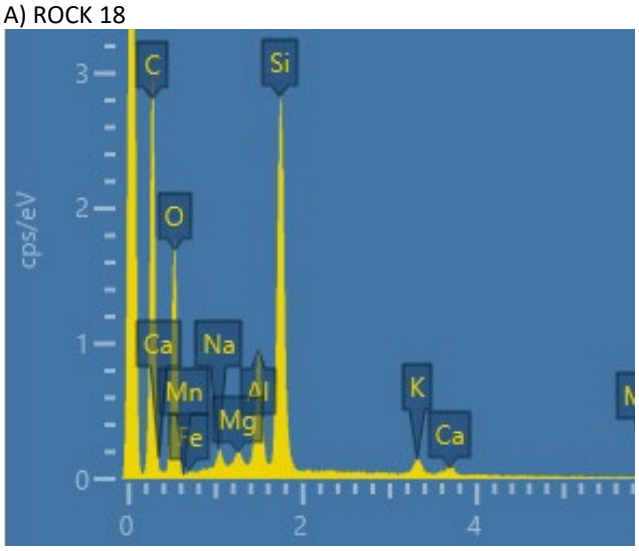

B) ROCK 18

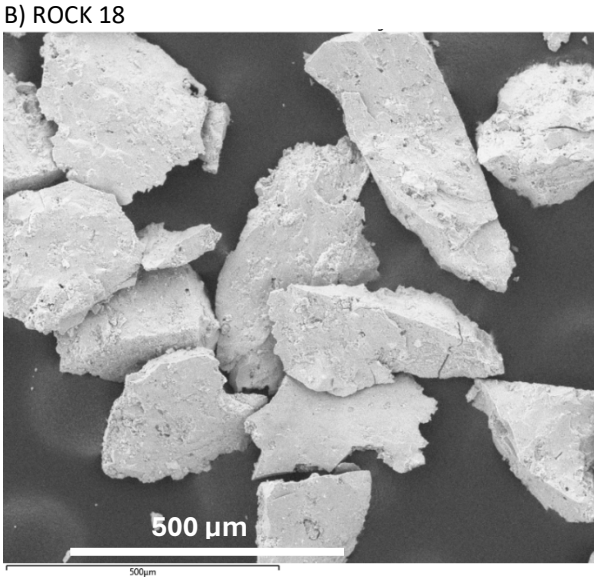

Figure S22. EDS-SEM data for volcanic Rock 18. EDS spectra (left) showing the presence of K. Backscatter SEM images (right) of grains from sieved and crushed rock slices from CA21P1.

9. Dose rate modeling for rocks

Dose rate with depth models for limestone rocks were calculated using the method of Jenkins et al. (2018) and Riedesel and Autzen (2020). The method of Jenkins et al. uses the approach of Aitken (1985, Appendix H) and Freiesleben et al. (2015) where the beta dose with depth (x) into a rock is calculated as:

$$\dot{D}(x)_{\beta}^{Rock} = \dot{D}_{Rock,\beta}^{inf}\left[1 - 0.5\left(e^{-bx} + e^{-b(h-x)}\right)\right] + \dot{D}_{Sed,\beta}^{inf}0.5(e^{-bx} + e^{-b(h-x)}) \qquad (1)$$

Here, *b* is the beta attenuation factor (1.9 mm^{-1}) following Sohbati et al. (2015) and $\dot{D}_{Rock,\beta}^{inf}$ and $\dot{D}_{Sed,\beta}^{inf}$ are the infinite matrix beta dose rates for the rock and sediment, respectively. The same equation is used to calculate the gamma dose rate with depth, ($\dot{D}(x)_{\gamma}^{Rock}$, and this uses a gamma attenuation factor of 0.02 mm^{-1}, which is density-corrected for an assumed rock density of 2.6 g/cm^2. The sediment alpha contribution is ignored, due to the short distances (~10 mm) travelled by alpha particles, and the alpha contribution arising from the gravel is calculated using an a-value of 0.15 ±

0.05 (Balescu and Lamothe, 1994). Calculated total dose rates of the more recent Reidesel and Autzen (2020) approach are lower than those of Jenkins et al. (2018).

A) Rock 2 (63-90 µm), Jenkins et al. (2018)

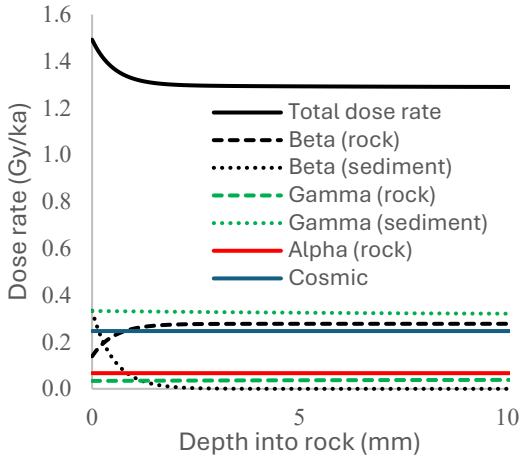

B) Rock 2 (63-90 µm), Riedesel & Autzen (2020)

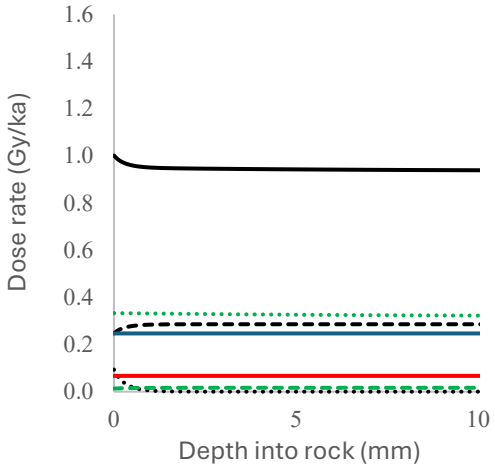

C) Rock 2 (90-125 µm), Jenkins et al. (2018)

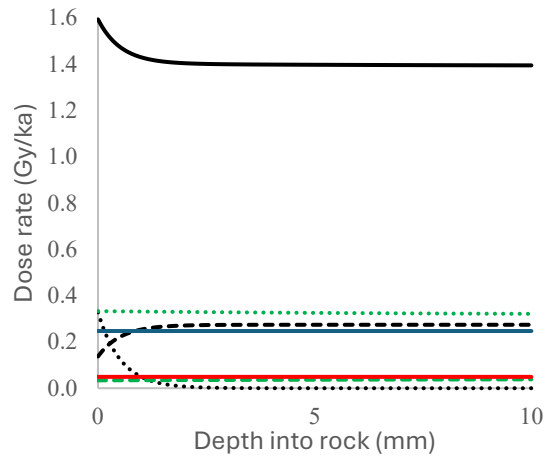

D) Rock 2 (90-125 µm), Riedesel & Autzen (2020)

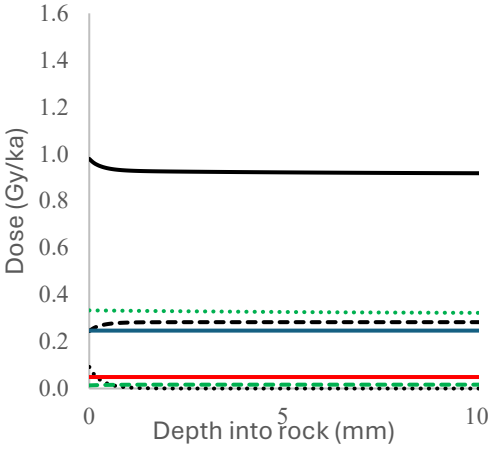

E) Rock 10 (125-180 µm), Jenkins et al. (2018)

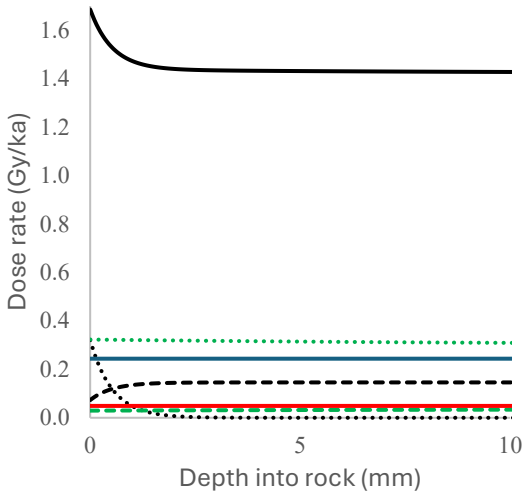

F) Rock 10 (125-180 µm), Riedesel & Autzen (2020)

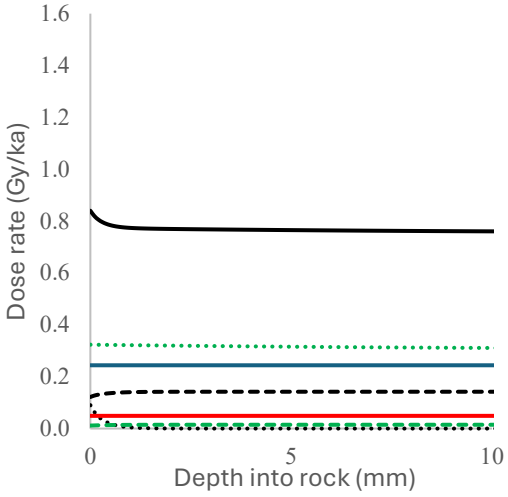

G) Rock 18 (180-250 µm), Jenkins et al. (2018) H) Rock 18 (180-250 µm), Riedesel & Autzen (2020)

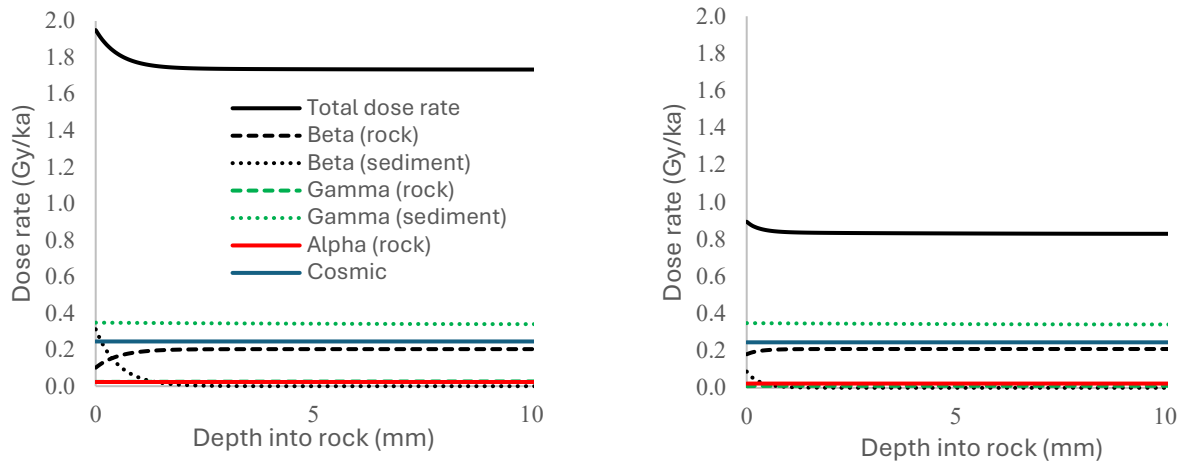

Figure S23. A comparison of two dose rate with depth models for limestone rocks from CV21P1.

10. Statistical models for calculating sample D_e and their assumptions

Central Dose Model

The central dose model (CDM or CAM) assumes that the sample has been completely re-set by sunlight prior to burial (Galbraith et al.,1999). The CAM estimates a "geometric weighted mean" from logged *De* distributions (i.e., the x-axis of the Kernel density estimate distribution is logged). The *De* distributions are logged prior to mean calculation, because *De* values tend to correlate positively with *De* errors (adding to positive skewness in the unlogged *De* distribution), so CAM is an attempt to avoid age over-estimations resulting from this positive skew.

Minimum Dose Model

The minimum dose model (MDM or MAM), is applied to samples thought to have been partially bleached leading to a truncated log-normal *De* distribution with a positive skew (Galbraith et al.,1999). The MAM calculates a *De* estimate from the lower (younger) limb of the distribution to estimate the most recent bleaching event.

Average Dose Model

The average dose model, or ADM, is applied to samples that: i) are thought to be fully bleached prior to burial, and ii) are affected by a heterogeneous dose rate environment at the grain-scale (Guérin et al., 2017). These heterogeneities are typically associated with "hot" spots generated by K-rich feldspar grains. Modeling suggests that hotspots should lead to positively skewed *De* distributions (Mayya et al., 2006). On a positively skewed *De* distribution, the calculated ADM *De* value will always be higher than the CAM *De* value.

The authors of the ADM model argue that an age should be calculated using an *average De* value, rather than a *geometric* mean *De* value (like CAM) because we divide our sample *De* value by an *average* dose rate (measured by ICP-MS or gamma spectrometry, for example) to obtain an age. Due to the limits of our technology, we cannot measure the *single-grain dose rate* distribution—just an *average dose rate* for the sample. Therefore, they believe that the traditional method of dividing a geometric weighted mean *De* value (CAM) by an average dose rate will lead to an age underestimate.

11. D_e-depth profiles from volcanic rocks

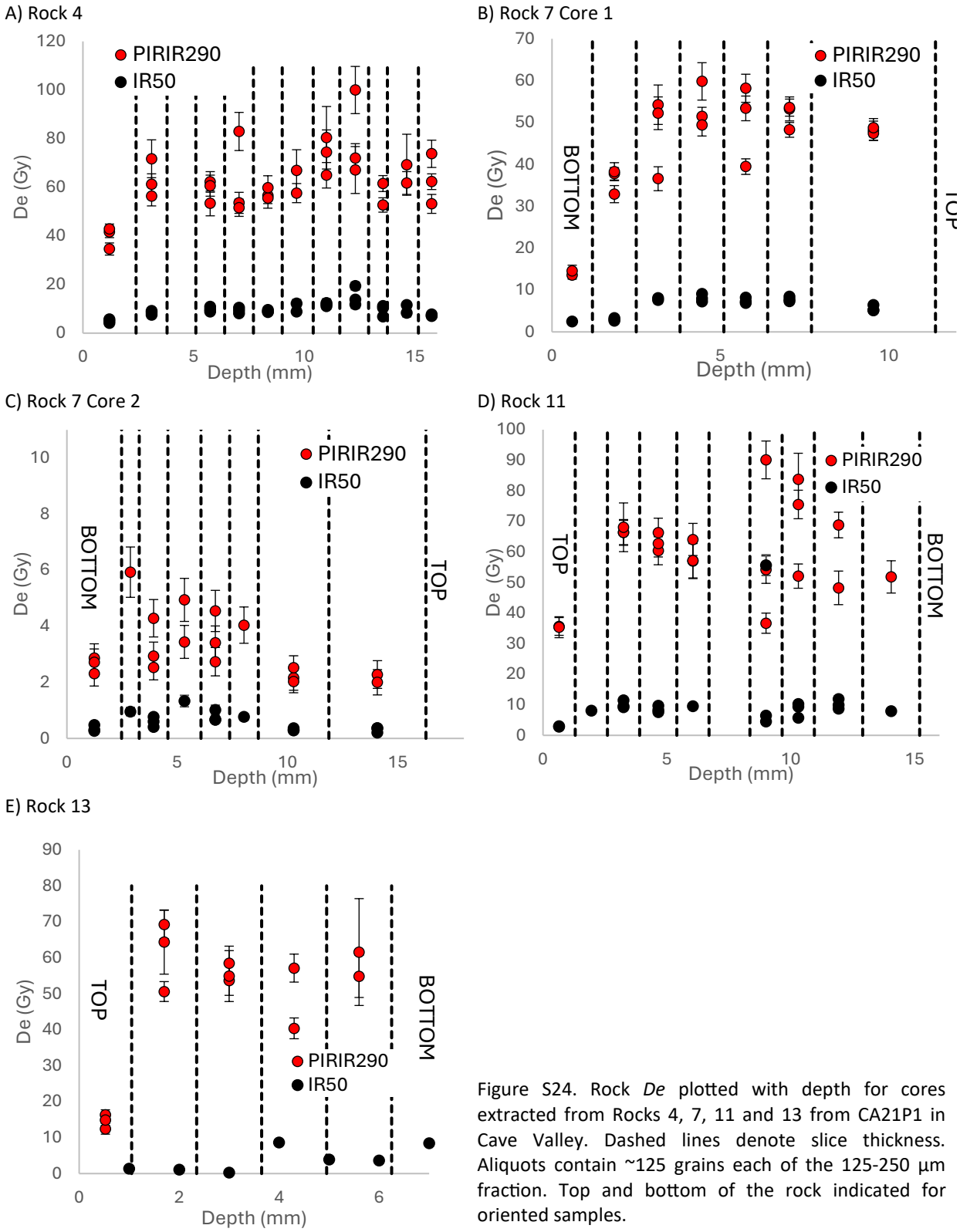

Figure S24. Rock *De* plotted with depth for cores extracted from Rocks 4, 7, 11 and 13 from CA21P1 in Cave Valley. Dashed lines denote slice thickness. Aliquots contain ~125 grains each of the 125-250 µm fraction. Top and bottom of the rock indicated for oriented samples.

A) Rock 18 Core 1

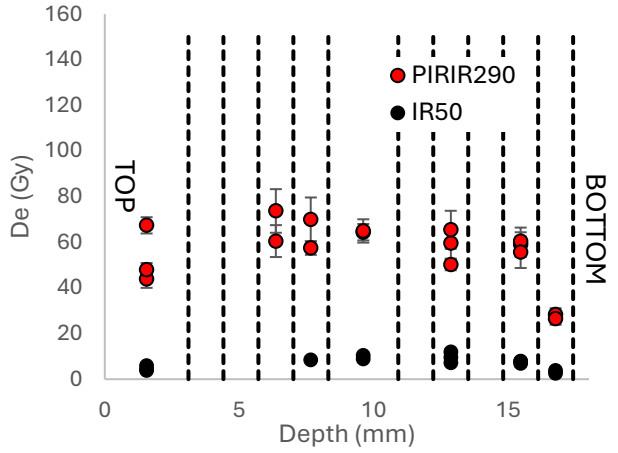

B) Rock 18 Core 2

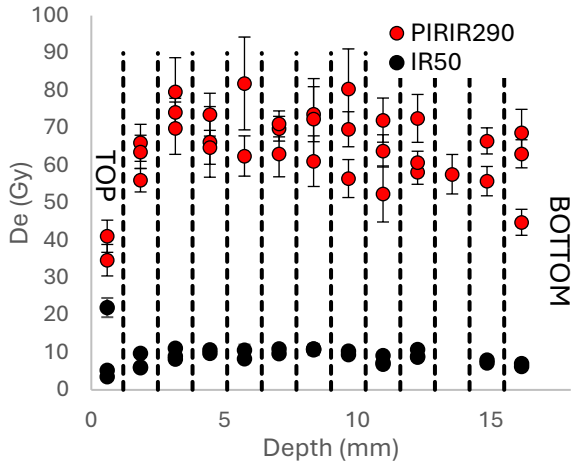

C) Rock 18 Core 3

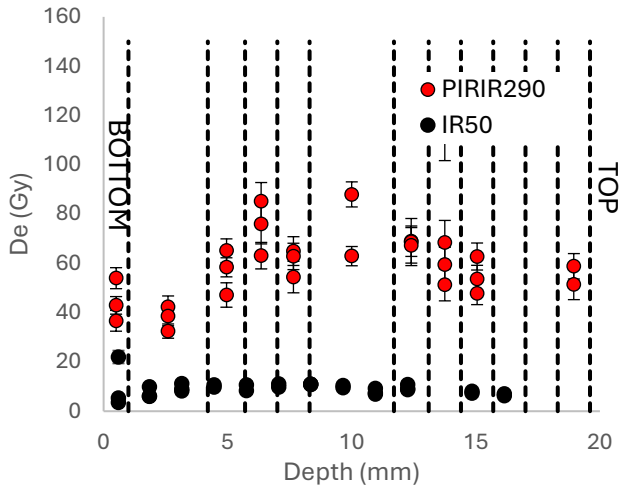

Figure S25. *De* plotted with depth for 3 cores extracted from Rock 18 from CA21P1 in Cave Valley. Dashed lines denote slice thickness. Aliquots contain ~125 grains each of the 125-250 µm fraction. Top and bottom of the rock indicated for oriented samples.

References

Aitken, JM (1985) Thermoluminescence Dating. Academic Press, London.

Auclair, M, Lamothe, M, Huot, S (2003) Measurement of anomalous fading for feldspar IRSL using SAR. Radiation Measurements 37: 487-492.

Balescu, S, Lamothe, M (1994) Comparison of TL and IRSL age estimates of feldspar coarse grains from waterlain sediments. Quaternary Science Reviews 13(5-7): 437-444.

Bulur, E (1996) An alternative technique for optically stimulated luminescence (OSL) experiment. Radiation Measurements 26: 701-709.

Crafford, AEJ (2007) Geologic Map of Nevada: U.S. Geological Survey Data Series 249, 1 CD-ROM, 46 p., 1 plate.

Dietze, M (2021) plot_KDE(): Plot kernel density estimate with statistics. Function version 3.6.0. In: Kreutzer, S, et al. (2021) Luminescence: Comprehensive Luminescence Dating Data Analysis. R package version 0.9.14. https://CRAN.R-project.org/package=Luminescence

Dietze, M, Kreutzer, S (2021) plot_AbanicoPlot(): Function to create an Abanico Plot.. Function version 0.1.15. In: Kreutzer, S et al. (2021) Luminescence: Comprehensive Luminescence Dating Data Analysis. R package version 0.9.14. https://CRAN.R-project.org/package=Luminescence

Freiesleben, T, Sohbati, R, Murray, A, Jain, M, Khasawneh, S, Hvidt, S, Jakobsen, B (2015) Mathematical model quantifies multiple daylight exposure and burial events for rock surfaces using luminescence dating. Radiation Measurements 81: 16-22.

Galbraith, RF, Roberts, RG, Laslett, GM, Yoshida, H, Olley, JM (1999) Optical dating of single and multiple grains of quartz from Jinmium rock shelter, northern Australia: Part I, experimental design and statistical models. Archaeometry 41: 339-364.

Guérin, G, Christophe, C, Philippe, A, Murray, AS, Thomsen, KJ, Tribolo, C, Urbanova, P, Jain, M, Guibert, P, Mercier, N, Kreutzer, S, and Lahaye, C (2017) Absorbed dose, equivalent dose, measured dose rates, and implications for OSL age estimates: Introducing the Average Dose Model. Quaternary Geochronology 41: 163-173.

Huntley, DJ, Lamothe, M (2001) Ubiquity in anomalous fading in K-feldspars and the measurement and correction for it in optical dating. Canadian Journal of Earth Science 38: 1093-1106.

Huntley, DJ, Lian, OB (2006) Some observations on tunneling of trapped electrons in feldspars and their implications for optical dating. Quaternary Science Reviews 25: 2503-2512.

Jenkins, GTH, Duller, GAT, Roberts, HM, Chiverrell, RC, Glasser, NF (2018) A new approach for luminescence dating glaciofluvial deposits – High precision optical dating of cobbles. Quaternary Science Reviews 192: 263-273.

Kars, RH, Wallinga, J, Cohen, KM (2008) A new approach towards anomalous fading correction for feldspar IRSL dating — tests on samples in field saturation. Radiation Measurements 43: 786-790.

Mayya, YS, Morthekai, P, Murari, MK, Singhvi, AK (2006) Towards quantifying beta microdosimetric effects in single-grain quartz dose distribution. Radiation Measurements 41: 1032-1039.

Murray, A, Buylaert, J-P, Thiel, C (2015) A luminescence dating intercomparison based on a Danish beach-ridge sand. Radiation Measurements 81: 32-38.

Riedesel, S, Autzen, M (2020) Beta and gamma dose rate attenuation in rocks and sediment. Radiation Measurements 133: 106295.

Roberts, HM (2007) Assessing the effectiveness of the double-SAR protocol in isolating a luminescence signal dominated by quartz. Radiation Measurements 42: 1627-1636.